

Article

Microstructure, Wear Resistance and Corrosion Performance of Inconel 625 Layer Fabricated by Laser/Ultra-High Frequency (UHF) Induction Hybrid Deposition

Rui Sun ^{1,*}, Yuhang Qiao ¹, Xinhong Li ², Yongjun Shi ³ and Xiaogang Wang ⁴

¹ College of Mechanical and Automotive Engineering, Qingdao University of Technology, Qingdao 266520, China

² College of Resources Engineering, Xi'an University of Architecture and Technology, Xi'an 710055, China

³ College of Mechanical and Electronic Engineering, China University of Petroleum, Qingdao 266580, China

⁴ Shengli Oilfield Technology Inspection Center, SINOPEC, Dongying 257000, China

* Correspondence: sunrui_92@126.com

Abstract: In order to avoid microstructure degradation caused by low frequency induction heat in laser-induction hybrid deposition, this paper proposes a laser/ultra-high frequency (UHF) induction hybrid deposition method. Microstructure observation is carried out to reveal the effect of UHF induction heat on the microstructure of the deposited layer. Results indicate that the laser-UHF induction hybrid deposited layer, under a current density of $1.14 \times 10^8 \text{ A/m}^2$, exhibits a finer microstructure and fewer Laves phases than that of the laser deposited layer. As the current density increases from $1.01 \times 10^8 \text{ A/m}^2$ to $1.14 \times 10^8 \text{ A/m}^2$, the microstructure of the laser-UHF induction hybrid deposited layer is significantly refined; however, as the current density further increases, the microstructure is only slightly further refined, since the enhanced thermal effect, along with the increasing current density, may help grain growth. Wear test demonstrates that the laser-UHF induction hybrid deposited layer obtained with a current density of $1.40 \times 10^8 \text{ A/m}^2$ has the lowest average friction coefficient of 0.375 and the lowest wear rate of $15.53 \times 10^{-5} \text{ mm}^3/\text{N}\cdot\text{m}$, indicating a better wear resistance. Corrosion resistance is also evaluated by electrochemical corrosion test. Results indicate that the addition of UHF induction heat improves the corrosion resistance of the deposited layer. Owing to the high ohm resistance of the passive film, the deposited layer fabricated with a current density of $1.01 \times 10^8 \text{ A/m}^2$ exhibits the best corrosion resistance. Based on the analysis of wear and corrosion performance, the current density of $1.40 \times 10^8 \text{ A/m}^2$ is an optimal parameter for a laser-UHF induction hybrid deposited Inconel 625 layer.

Keywords: ultra-high frequency (UHF) induction heat; laser deposition; microstructure; wear resistance; corrosion resistance



Citation: Sun, R.; Qiao, Y.; Li, X.; Shi, Y.; Wang, X. Microstructure, Wear Resistance and Corrosion Performance of Inconel 625 Layer Fabricated by Laser/Ultra-High Frequency (UHF) Induction Hybrid Deposition. *Processes* **2023**, *11*, 1118. <https://doi.org/10.3390/pr11041118>

Academic Editor: Prashant K. Sarswat

Received: 15 March 2023

Revised: 1 April 2023

Accepted: 3 April 2023

Published: 5 April 2023



Copyright: © 2023 by the authors. Licensee MDPI, Basel, Switzerland. This article is an open access article distributed under the terms and conditions of the Creative Commons Attribution (CC BY) license (<https://creativecommons.org/licenses/by/4.0/>).

1. Introduction

Laser deposition has been proven to be an effective and low-cost method of repairing components with surface defects. Many scholars have conducted in-depth research on layer materials, process parameters, and performance of laser deposited layers [1–3]. Although this research can provide relatively reliable guidance for the practical application of laser deposition, this method is still not widely available in industrial production. The inner micro-crack in deposited layers is the critical obstacle to the wide application of laser deposition.

Existing studies indicates that the micro-cracks in laser deposited layers are mainly caused by the large temperature gradient between substrate and layers during deposition, as well as the significant difference in their thermo-physical properties [4–6]. Given that thermo-physical properties are intrinsic characteristics of materials, researchers generally reduce the occurrence of micro-cracks by optimizing the temperature gradient between

substrate and deposited layers. In fact, optimization of the temperature gradient inhibits micro-cracks by decreasing residual stress in the deposited layers, especially in the transition region between deposited layer and substrate. This has been identified as a feasible method to optimize the temperature gradient by using an auxiliary heat source, such as resistance heat or induction heat, in order to preheat the substrate during laser deposition. Induction heat, which uses an alternating magnetic field to generate heat energy, has recently become a better choice as auxiliary heat source, due to its excellent heating efficiency and non-contact heating method. Zhou et al. [7,8] utilized induction heat to preheat the substrate during laser deposition, referred to as the laser-induction hybrid deposition (LIHD) method, and microstructure observation indicated that the micro-cracks could be effectively eliminated by the preheating effect of the induction heat on the substrate. Research carried out by Farahmand et al. [9] showed that induction heat avoids stress concentration by decreasing the temperature gradient during deposition, which further diminishes the crack sensitivity of the deposited layer. In addition, the introduction of induction heat to laser deposition increases the deposition rate when compared to conventional laser deposition. Dalae et al. [10] found that the LIHD method has about three times the deposition rate of the laser deposition method.

However, current research on the LIHD method usually employs induction heat with a current frequency lower than 100 kHz. According to induction heating theory, induction heat with a low current frequency is of poor controllability and has a large heat affected zone. Consequently, the molten metal during LIHD is usually overheated when using low or medium frequency induction heat to reduce the temperature gradient. The overheating of molten metal will cause microstructure degradation in the deposited layer, which further weakens its performance, such as its mechanical properties and corrosion resistance. Meng et al. [11] fabricated a Ni-based alloy layer without microcracks by the LIHD method, but the secondary dendrites' arm space of the layer was significantly increased compared with that of a laser deposited layer. Wang et al. [12,13] reported that the addition of induction heat aggravates the heat effect suffered by molten metal during deposition, resulting in heat damage to the ceramic particle reinforcement phases in the deposited layer. The microhardness and wear resistance of the deposited layer consequently decreased. Therefore, the advantage of the current LIHD method is mostly limited to inhibiting microcracks, and microstructure degradation of the deposited layer cannot be completely avoided.

With the development of induction heating technology, the current frequency of induction heat is greatly increased. Ultra-high frequency (UHF) induction heat, with a current frequency higher than 700 kHz, is of good controllability and has a small heat-affected zone. UHF induction heat has recently been applied in the precision forming field, such as metal powder production [14], precision welding [15,16] and rapid sintering of nanocomposites [17]. In view of the technological superiority of UHF induction heat, the microstructure degradation that occurs during temperature gradient optimization may be prevented by introducing UHF induction heat instead of low or medium frequency induction heat to laser deposition. In addition, since the induction coil used in UHF induction heating is commonly of a small dimension, the magnetic field near the molten pool generated during UHF induction heating is more intensive, compared with that generated during the conventional low or medium frequency induction heating process. The intensive magnetic field will produce a Lorentz force, which will further accelerate the metal flow in molten metal. Previous research has indicated that a violent flow in molten metal is helpful in microstructure refinement [18,19]. Therefore, the intensive electromagnetic field during UHF induction heating will also contribute to the microstructure refinement of the deposited layer.

In this paper, UHF induction heat is added to the laser deposition process, referred to as the laser-UHF induction hybrid deposition method. To examine the effect of UHF induction heat on the deposited layer, Inconel 625 metal layers are fabricated by the laser-UHF induction hybrid deposition method. The microstructure evolution of the deposited layer along with different intensities of UHF induction heat is analyzed. Key properties

of the deposited layer, including wear resistance and corrosion performance, are also evaluated. The findings of the present work are expected to provide effective reference for the application of the laser-UHF induction hybrid deposition method.

2. Experiment and Analysis Method

2.1. Experimental Platform and Deposition Process

A 316L stainless steel with a dimension of 60 mm × 30 mm × 4 mm is used as the substrate. Inconel 625 metal layers are deposited on the substrate by the laser-UHF induction hybrid deposition experimental platform. The chemical composition of the Inconel 625 powder and 316L stainless steel are listed in Table 1. The deposition platform, as shown in Figure 1, is mainly composed of a UHF induction heating module, laser heating module, powder-feed module and processing module. Figure 2 gives a detailed description of the deposition process. During deposition, the induction coil is coaxially arranged with the laser head. The metal powder passes through the center of the induction coil and is rapidly melted by the laser beam. With the motion of the substrate (v_s represents the moving velocity), the molten metal powder solidifies and forms the deposition layer. UHF induction heat also acts during the whole deposition process. As shown in Figure 2, a magnetic field is generated around the induction coil during deposition. Due to the spatial distribution characteristics of the magnetic field, the areas adjacent to the induction coil, including the molten pool, the deposited layer and the substrate, all undergo tUHF induction heat. Besides the UHF induction heat, the magnetic field also generates a Lorentz force, which will act on the high temperature metal in the molten pool. It should be noted that the UHF induction heat intensity and Lorentz force intensity will change with the distance between induction coil and target area. During the deposition experiment, the diameter d_1 and the winding diameter d_2 of the induction coil are 1 mm and 6 mm, respectively. The distance between induction coil and substrate h is adjusted to 3 mm. The deposition parameters used in the experiments are listed in Table 2. During deposition, each case listed in Table 2 is repeated three times, and the three layers that are deposited in the same parameters are then used to provide the test samples for the following test.

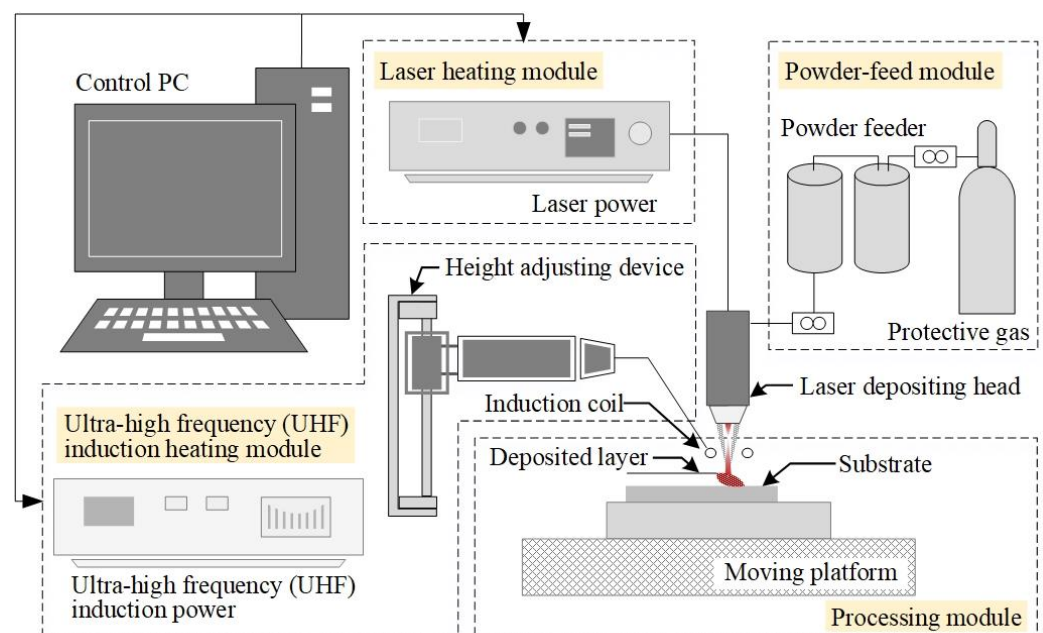


Figure 1. Schematic of laser-UHF induction hybrid deposition experimental platform.

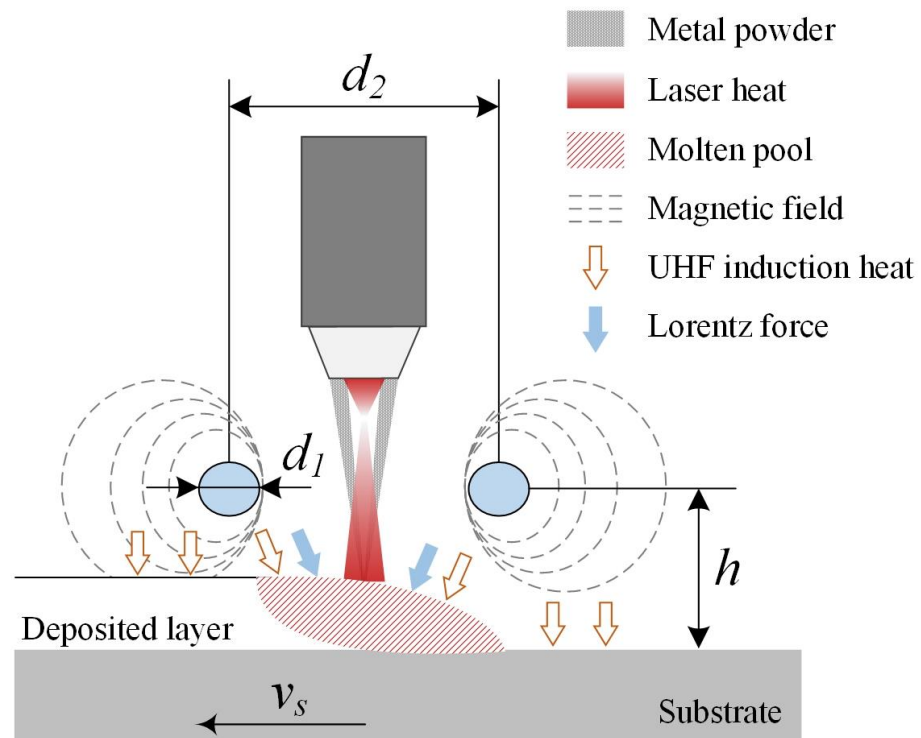


Figure 2. Schematic of the deposition process.

Table 1. Chemical composition of Inconel 625 powder and 316L stainless steel.

Materials	Ni	Cr	Si	Mo	Mn	Nb	Co	C	S	P	Fe
Inconel 625	≥ 58	20.0–23.0	≤ 0.5	8.0–10.0	≤ 0.5	3.15–4.15	≤ 1.0	≤ 0.015	≤ 0.008	≤ 0.024	Bal.
316L	10.0–14.0	16.0–18.0	≤ 1.0	2.0–3.0	≤ 2.0	–	–	≤ 0.03	≤ 0.03	≤ 0.045	Bal.

Table 2. Deposition parameters used in experiments.

Case	Laser Power P (W)	Laser Beam Diameter d (mm)	Powder Flow Rate m (g/min)	Current Frequency f (kHz)	Current Density I (A/m^2)	Moving Velocity v_s (mm/s)
1					1.01×10^8	
2					1.14×10^8	
3	700	1	5	850	1.27×10^8	6
4					1.40×10^8	
5				–	–	

2.2. Microstructure Analysis Method

After the deposition experiments, the experimental samples were cross-sectioned by a wire electrical charge machine. The cross-sections of these samples were ground by SiC abrasive paper with 400 to 2000 mesh, and then polished with the diamond suspension on a metallographic sample polishing machine. The microstructure of the samples was observed by a scanning electron microscope (SEM) equipped with energy disperse spectroscopy (EDS). Before the microstructure observation, the polished cross-sections were etched with aqua regia ($HNO_3:HCl = 1:3$) for 50 s to clearly reveal the microstructure morphology.

2.3. Wear Resistance Test

The wear resistance of the deposited layers was tested by a reciprocating friction wear tester (MFT-EC4000). The deposited layer was first ground to get a flat surface before the test. A silicon nitride (Si_3N_4) ceramic ball with a diameter of 9.525 mm was used to slide along the testing surface of the deposited layer along a straight path of 5 mm. The reciprocating sliding frequency of the ceramic ball and the load exerted on it were 2 Hz and 5 N, respectively. The friction wear test time of each deposited layer was 30 min and no lubricating substances were added during the test. After the test, the wear surface morphology and its 2D profile were observed and measured by a laser scanning confocal microscope (LSCM).

2.4. Corrosion Resistance Test

The corrosion performance of the deposited layers was evaluated by an electrochemical workstation equipped with a three-electrode system. During the testing process, a platinum plate was applied as the counter electrode, a saturated calomel electrode was applied as the reference electrode, and the deposited layer was used as the working electrode. The deposited layer was packaged in epoxy resin and then finely ground to expose a smooth testing surface with a dimension of 2 mm \times 6 mm before the test. Then, the three electrodes were immersed in a 3.5% NaCl electrolyte solution at room temperature. After the test, the electrochemical impedance spectroscopy (EIS) and potentiodynamic polarization were derived to reflect the corrosion performance of the deposited layers.

3. Results and Analysis

3.1. Microstructure Analysis

The service performance of the deposited layer is in large part determined by microstructure morphology; a fine microstructure morphology contributes to a better performance of the deposited layer. Figure 3 shows the SEM image of the cross-section of a laser-UHF induction hybrid deposited layer, which was prepared under a current frequency of 850 kHz and current density of 1.14×10^8 A/m². The thickness of the deposited layer is 0.631 mm. As shown in Figure 4, the element distribution along Line A—A' that stretches across the laser-UHF induction hybrid deposited layer and substrate is obtained by means of EDS detection. It can be seen that the element content gradually changed from the deposited layer to the substrate, which means that metallurgical bonding between the deposited layer and substrate is obtained. Figure 5 shows the microstructure in the top region of the deposited layer obtained by laser deposition and laser-UHF induction hybrid deposition method. The laser-UHF induction hybrid deposited layer was obtained with a current frequency of 850 kHz and current density of 1.14×10^8 A/m². According to Figure 3, the top region of the laser deposited layer is mainly composed of coarse cellular grains, and the maximum dimension of these cellular grains is up to 7.8 μm , while in the top region of the laser-UHF induction hybrid deposited layer the microstructure consists of almost equiaxed grains, and the dimension of these equiaxed grains averages 4.82 μm , which means that the laser-UHF induction hybrid deposited layer has a more refined microstructure compared with the laser deposited layer. According to induction heating theory, there is an intensive electromagnetic field during UHF induction heating, which generates a Lorentz force in the molten pool. The Lorentz force has a significant stirring effect on the molten pool, breaking down the developing grains in its solidifying front. Therefore, the nucleation rate is increased, which means a microstructure with fine grain size is obtained.

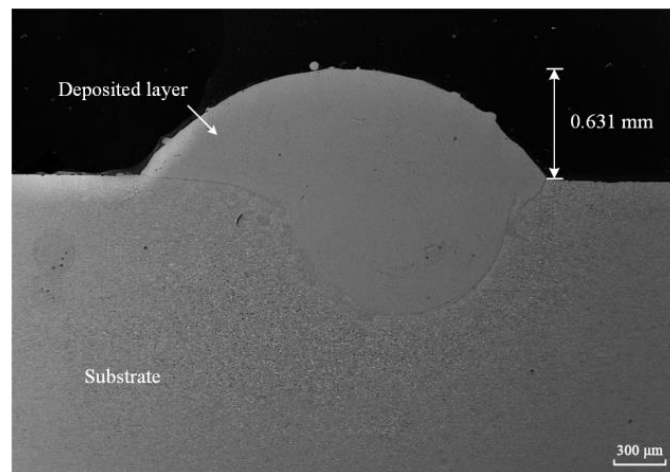


Figure 3. SEM image of the cross-section of laser-UHF induction hybrid deposited layer.

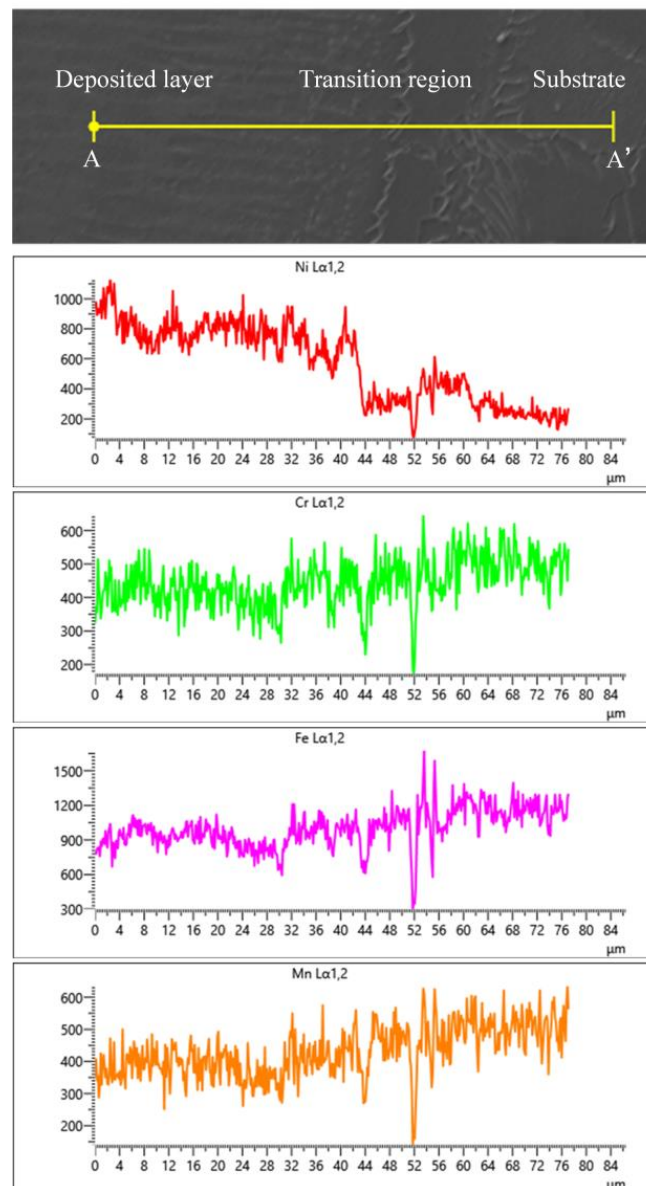


Figure 4. Element distribution from the laser-UHF induction hybrid deposited layer to the substrate.

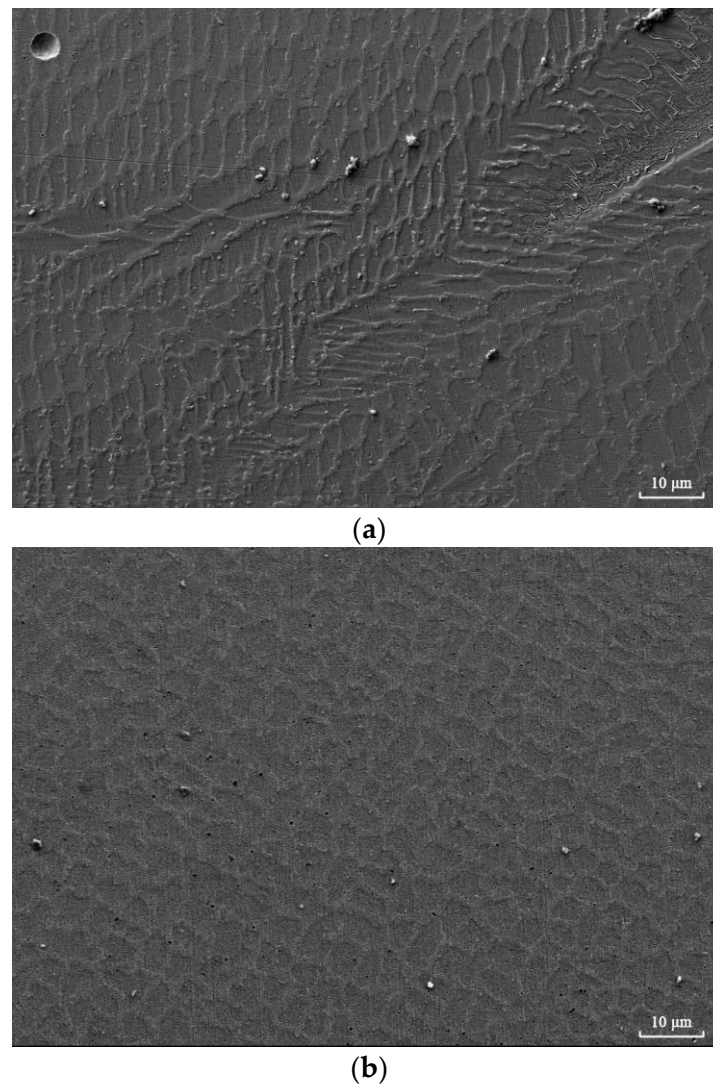


Figure 5. Microstructure in the top region of the deposited layer obtained by (a) laser deposition method and (b) laser-UHF induction hybrid deposition method.

Figures 6 and 7 show the EDS analysis of the top region of the laser deposited layer and laser-UHF induction hybrid deposited layer, respectively. According to the high magnification SEM images of the detected zone shown in Figures 6a and 7a, some white precipitated phases are distributed in the intergranular regions. The element maps depicted in Figures 6b–e and 7b–e show that these white precipitated phases are Laves phases, which are enriched in Nb and Mo. By means of the image processing techniques, the volume fraction of the Laves phases in the detected region is calculated. Results indicate that the volume fraction of the Laves phases for the detected region of the laser-UHF induction hybrid deposited layer and the laser deposited layer are 5.47% and 7.15%, respectively. This demonstrates that the addition of UHF induction heat is helpful in inhibiting the segregation of Nb and Mo. The inhibition of Nb and Mo segregation should be attributed to the electromagnetic stirring effect generated by the UHF induction heat. Previous research has shown that the electromagnetic stirring contributes not only to the grain refinement, but also to the uniform distribution of the alloying element, which inhibits the element segregation [20,21].

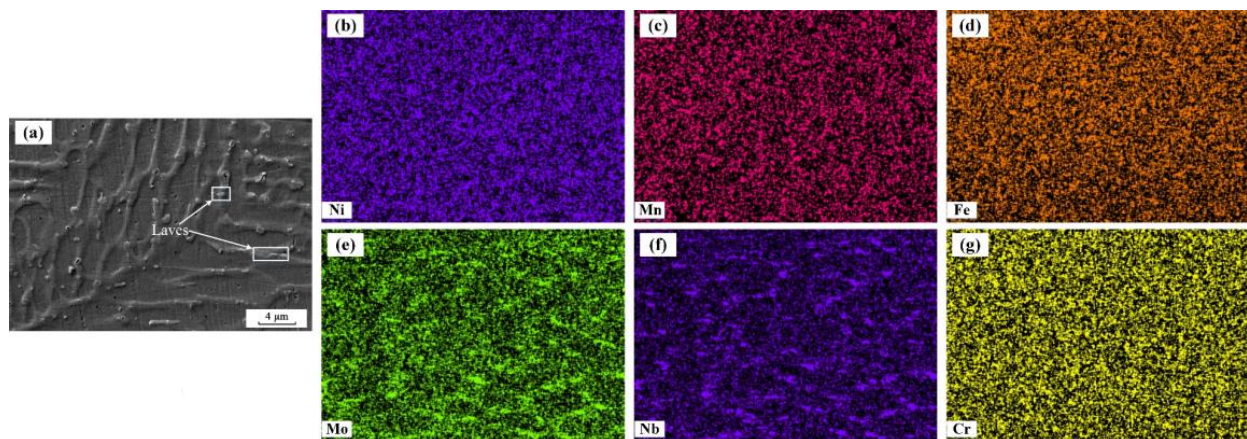


Figure 6. EDS analysis of the top region of laser deposited layer: (a) detected region (b–g) element maps of Ni, Mn, Fe, Mo, Nb and Cr.

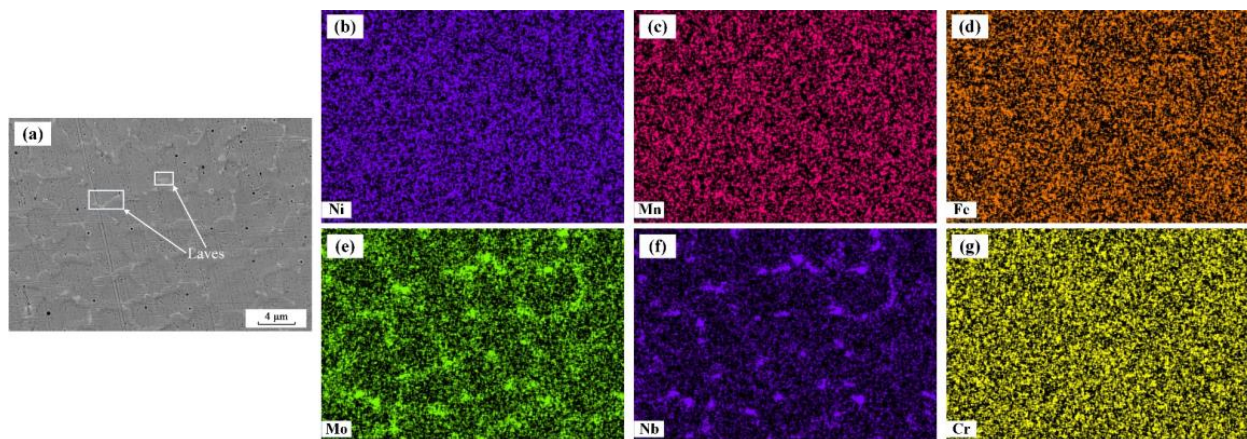


Figure 7. EDS analysis of the top region of laser-UHF induction hybrid deposited layer: (a) detected region (b–g) element maps of Ni, Mn, Fe, Mo, Nb and Cr.

Figure 8 further presents the microstructure in different regions of the laser-UHF induction hybrid deposited layer. Compared with the top region, where there are mostly equiaxed grains, the microstructure in the middle region of the laser-UHF induction hybrid deposited layer mainly exhibits columnar, with secondary dendrite, arms. The primary dendrite spacing and secondary dendrite arm spacing of the columnar dendrites are about $3\ \mu\text{m}$ and $2\ \mu\text{m}$, respectively. In the bottom region, the microstructure mainly consists of epitaxial elongated columnar grains, and the growth of the secondary dendrite arm seems to be inhibited in this region. The microstructure variation in different regions of the laser-UHF induction hybrid deposited layer should be attributed to the thermal conditions in different regions of the molten pool. During deposition, the molten metal in the bottom region of the molten pool is of a high temperature gradient and rapid cooling rate. Thus, the mushy zone where the epitaxial elongated columnar grains grows is intensively depressed. The development of the lateral branching of the columnar grains is consequently inhibited, therefore the secondary dendrite arms seldom appear in the bottom region. In the middle region of the molten pool, the temperature gradient and cooling rate of the molten metal are both decreased compared with that in the bottom region, and the development of the lateral branching of the columnar grains is encouraged, leading to significant growth of the secondary dendrite arms, while in the top region the molten metal is of a lower temperature gradient and higher cooling rate, so equiaxed grains consequently appear in this region.

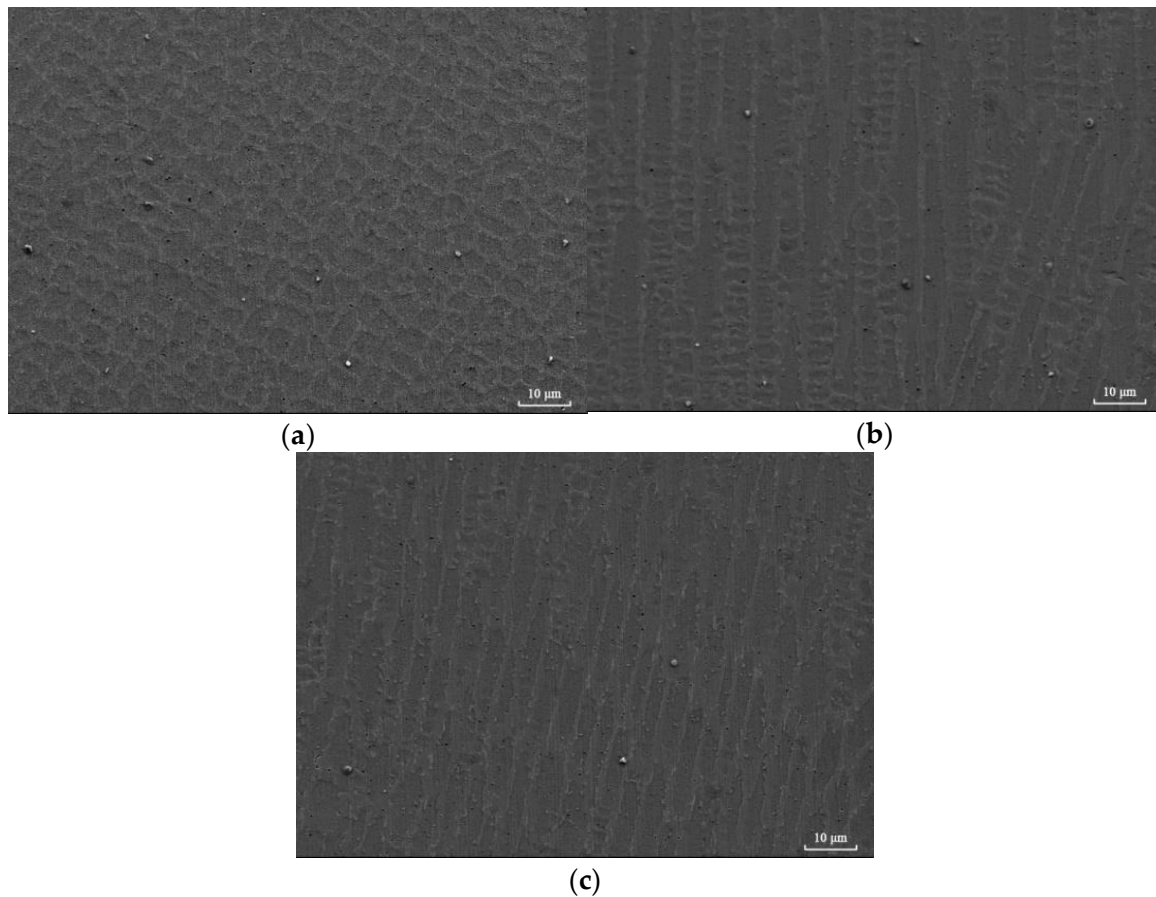


Figure 8. Micro-structure of the laser-UHF induction hybrid deposited layer in (a) top region, (b) middle region and (c) bottom region.

The current density is one of the key processing parameters for UHF induction heating. Figure 9 presents the thickness of the deposited layer, and it can be seen that the thickness varies from 0.601 mm to 0.675 mm, and the effect of current density on the thickness of the deposited layer is not so evident. Figure 10 depicts the microstructure in the top region of the laser-UHF induction hybrid deposited layers under different current densities. It is noticed that the equiaxed grains are the dominant microstructure morphology in the top region of the deposited layer under the four conditions. Comparison of the microstructure in the four conditions shows that the microstructure under current density of $1.01 \times 10^8 \text{ A/m}^2$ is significantly coarser than that under the other three conditions. According to the measured results, the grain size under a current density of $1.01 \times 10^8 \text{ A/m}^2$ is about $5.32 \mu\text{m}$. As the current density increases, the grain size decreases, but the decreasing scale is not so evident. The measured results indicate that the differences in grain size under a current density of $1.14 \times 10^8 \text{ A/m}^2$, $1.27 \times 10^8 \text{ A/m}^2$ and $1.40 \times 10^8 \text{ A/m}^2$ are about $4.12 \mu\text{m}$, $3.85 \mu\text{m}$ and $3.64 \mu\text{m}$, respectively. Based on the induction heating theory, the increasing current density means an intensive electromagnetic field, and the Lorentz force in the molten pool is thereby strengthened. Therefore, the stirring effect of the Lorentz force on the molten metal is enhanced, meaning that a fine microstructure can be obtained. However, the increasing current density also improves the UHF induction heat intensity, the thermal condition would be favorable to grain growth, and the refining effect of Lorentz force on the microstructure may be slightly weakened. Therefore, the decreasing scale of the grain size is not so significant as the current density increases from 1.14×10^8 to $1.40 \times 10^8 \text{ A/m}^2$.

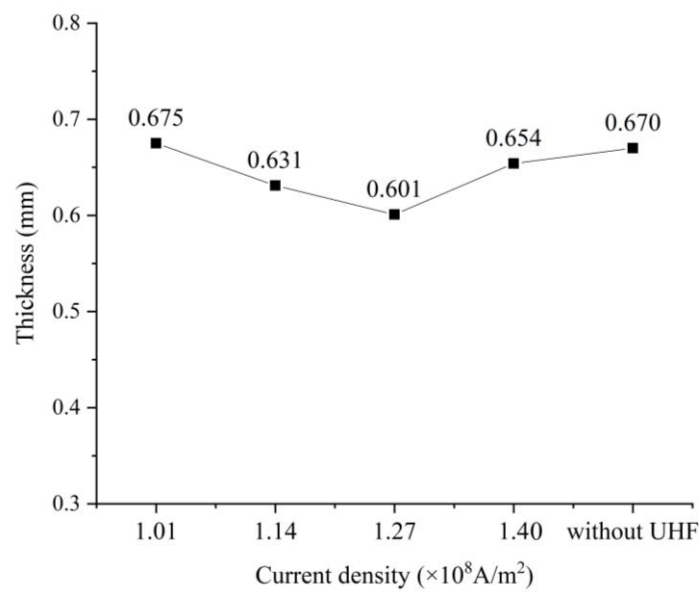


Figure 9. Thickness of the deposited layer.

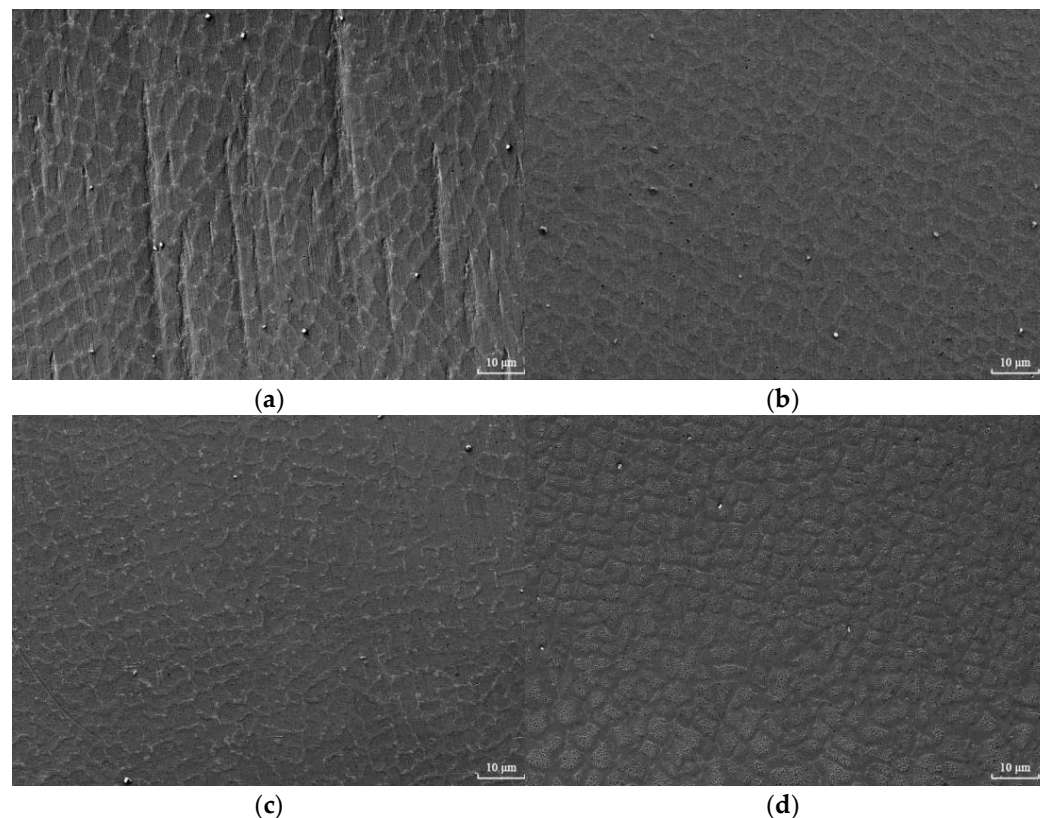


Figure 10. Microstructure in the top region of the laser-UHF induction hybrid deposited layers under current density of (a) $1.01 \times 10^8 \text{ A/m}^2$ (b) $1.14 \times 10^8 \text{ A/m}^2$ (c) $1.27 \times 10^8 \text{ A/m}^2$ (d) $1.40 \times 10^8 \text{ A/m}^2$.

3.2. Wear Resistance

Figure 11a,b are the friction coefficient curves and average friction coefficients of the laser-UHF induction hybrid deposited layers under the current density, respectively. According to Figure 11a, the friction coefficient of all the samples fluctuates drastically during the initial stages of the friction test. After about 5 min, the contact between the deposited layer and friction pair reaches a dynamic equilibrium state. Figure 11b demonstrates that, under the same friction test condition, the laser-UHF induction hybrid deposited

layer obtained at the current density of $1.01 \times 10^8 \text{ A/m}^2$ exhibits the highest average friction coefficient, while, as the current density increased to $1.40 \times 10^8 \text{ A/m}^2$, the average friction coefficient of the deposited layer decreased to 0.375. In addition, the deposited layer prepared by the current density of $1.14 \times 10^8 \text{ A/m}^2$ also exhibits a relatively low average friction coefficient of 0.404. The friction coefficient of the deposited layer prepared by a current density of $1.27 \times 10^8 \text{ A/m}^2$ is 0.525 is also lower than that of the deposited layer obtained at the current density of $1.01 \times 10^8 \text{ A/m}^2$. According to the analysis of the microstructure, this gradually becomes finer with increasing current density, which may contribute to the low friction coefficient. The average friction coefficient of the laser deposited layer (i.e., fabricated without UHF induction heat) is 0.514, which is about equal to that of the deposited layer obtained with a current density of $1.27 \times 10^8 \text{ A/m}^2$. However, based on the friction curves shown in Figure 11a, the friction curve of the laser deposited layer gradually increased to above 0.6 at the later stage of the friction test. In contrast, friction curves of the laser-UHF induction hybrid deposited layers are stable at the later stage of the friction test. The high friction coefficient of the laser deposited layer may also be caused by its relatively coarse microstructure.

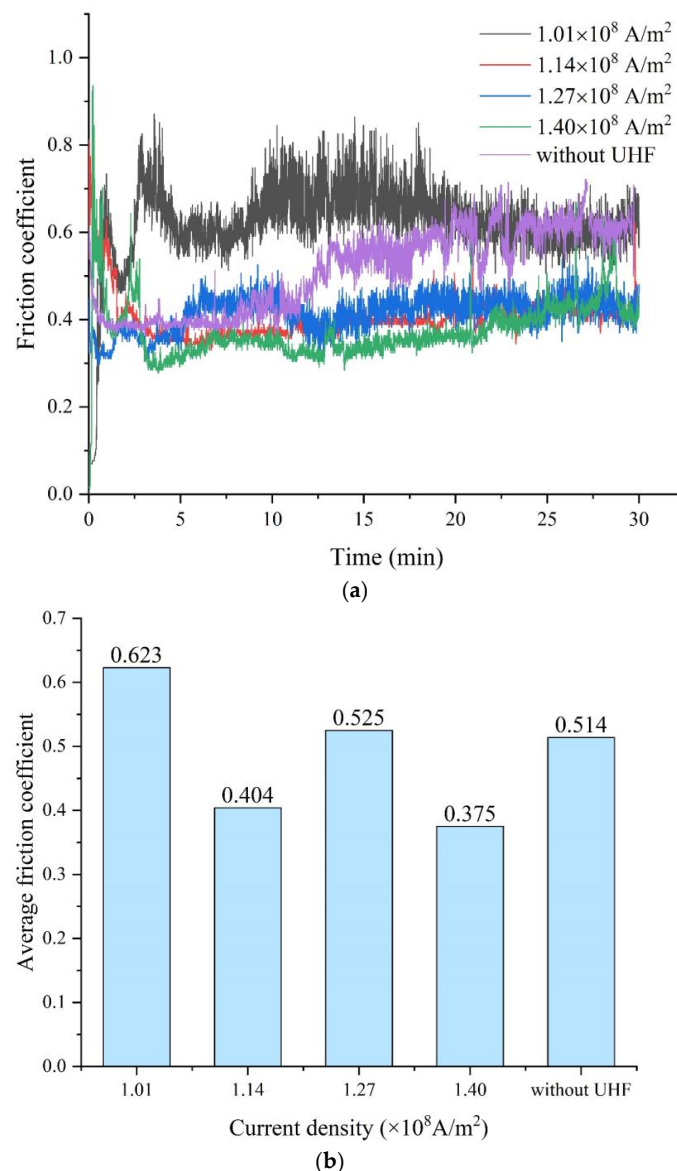


Figure 11. Friction coefficient curves (a) and average friction coefficients (b) of the laser-UHF induction hybrid deposited layers under different current densities.

The wear rate of the laser-UHF induction hybrid deposited layers was also evaluated, as shown in Figure 12. It can be seen that the deposited layers fabricated under the current density of $1.14 \times 10^8 \text{ A/m}^2$ and $1.40 \times 10^8 \text{ A/m}^2$ have a relatively low wear rate of 15.81×10^{-5} and $15.53 \times 10^{-5} \text{ mm}^3/\text{N}\cdot\text{m}$, respectively, indicating good wear resistance. However, the deposited layer obtained with the current density of $1.01 \times 10^8 \text{ A/m}^2$, which is of the highest friction coefficient among the tested layers, also shows the highest wear rate of $24.36 \times 10^{-5} \text{ mm}^3/\text{N}\cdot\text{m}$. The laser deposited layer exhibits a wear rate of $20.38 \times 10^{-5} \text{ mm}^3/\text{N}\cdot\text{m}$, which is slightly lower than that of the deposited layer prepared by the current density of $1.01 \times 10^8 \text{ A/m}^2$.

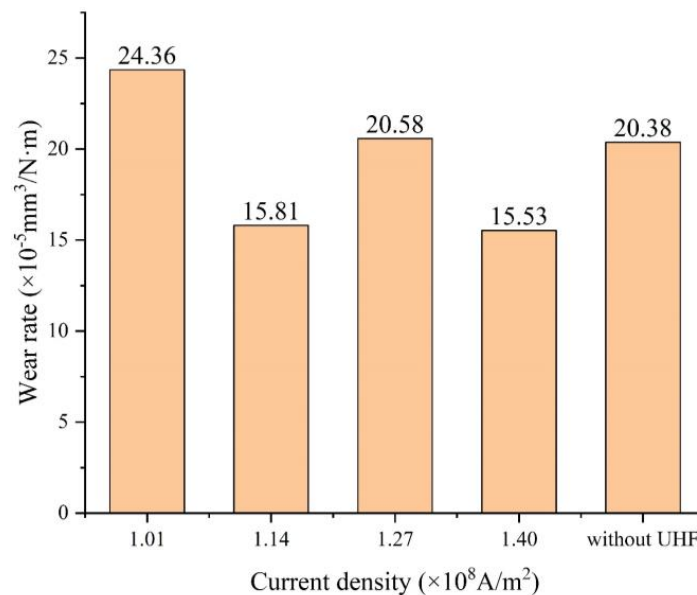


Figure 12. Wear rate of the laser–UHF induction hybrid deposited layers under different current densities.

The wear surface morphology and 2D profile of the wear surface morphology of the deposited layers are shown in Figure 13. Dense furrows along the sliding direction are observed in the wear surface of the deposited layers fabricated with a current density of $1.01 \times 10^8 \text{ A/m}^2$ and $1.27 \times 10^8 \text{ A/m}^2$, indicating an abrasive wear mechanism. The 2D profile of the wear surface morphology demonstrates that the wear track of the two layers is wide and deep. The wear surface morphology of the laser deposited layer also consists of dense furrows, therefore, the wear behavior in this condition is that of abrasive wear. Under abrasive wear condition, masses of wear debris peel off from the surface of the deposited layer, causing a high wear rate, while, for the layers that obtained with a current density of $1.14 \times 10^8 \text{ A/m}^2$ and $1.40 \times 10^8 \text{ A/m}^2$, the wear surface not only consists of furrows, but also of extensive pits. This means that the surface of the two deposited layers has adhesive wear and abrasive wear. These pits adhere to the wear surface, which plays a role in protecting it [22]. The dimension of the 2D profile of the wear surface morphology also indicates that the wear tracks of the two deposited layers are narrower than that of the other deposited layers, which also demonstrates the good wear resistance of the layers obtained with the current density of $1.14 \times 10^8 \text{ A/m}^2$ and $1.40 \times 10^8 \text{ A/m}^2$.

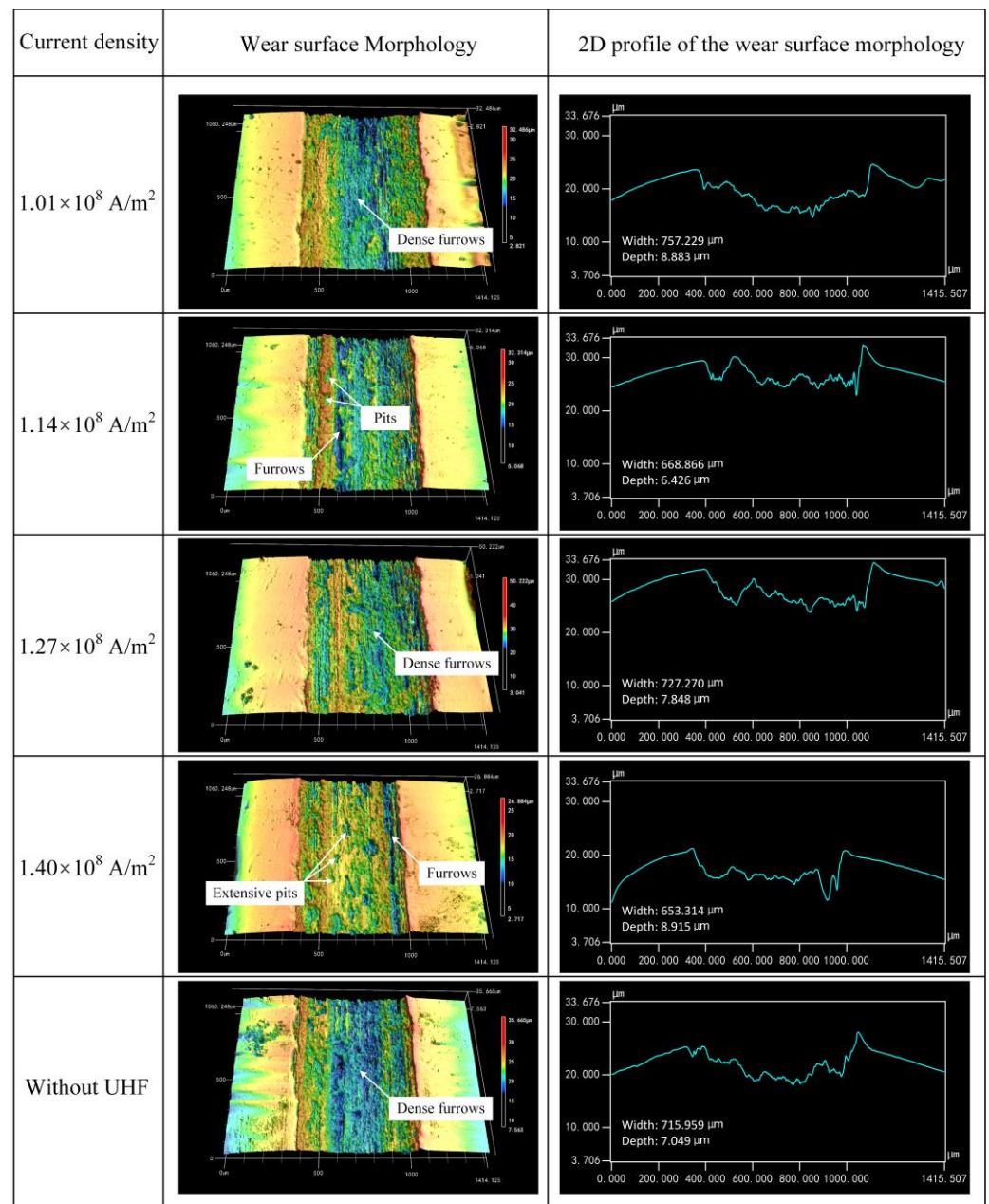


Figure 13. Wear surface morphology (left) and 2D profile of the wear surface morphology (right) of the laser-UHF induction hybrid deposited layers under different current densities.

3.3. Corrosion Resistance

Inconel 625 alloy has been broadly applied in offshore or subsea equipment due to its excellent corrosion resistance [23]. The base element of Inconel 625 alloy is nickel, which contributes to the corrosion resistance of the deposited layer. Current research on anticorrosive layers, especially in high entropy alloys, have shown that a certain amount of nickel exhibits good corrosion resistance [24]. To figure out the effect of current density on corrosion resistance, electrochemical corrosion tests were conducted for the deposited layers prepared with different current densities. Figure 14 depicts the polarization curves obtained from the electrochemical corrosion tests. According to the polarization curves, the corrosion potential (E_{corr}), corrosion current density (E_{corr}) and breakdown potential (E_b) are reported in Table 3. A lower corrosion potential means that corrosion more easily occurs at the metal surface. Experimental results indicate that the layer deposited under the current density of $1.01 \times 10^8 \text{ A/m}^2$ has the highest corrosion potential of -359 mV , while the layer deposited

under the current density of $1.27 \times 10^8 \text{ A/m}^2$ exhibits the lowest corrosion potential of -394 mV . The laser deposited layer has a corrosion potential of -387 mV , which is lower than that of the laser-UHF induction hybrid deposited layer obtained with the current densities of $1.01 \times 10^8 \text{ A/m}^2$, $1.14 \times 10^8 \text{ A/m}^2$ and $1.40 \times 10^8 \text{ A/m}^2$. Poloczek et al. [25] and Rezayat et al. [26] also carried out corrosion tests for laser deposited Inconel 625 layers, in which the corrosion potential E_{corr} was -377 mV and -390 mV , respectively. According to the corrosion data for laser-UHF induction hybrid deposited layers, it can also be seen that under current densities of $1.01 \times 10^8 \text{ A/m}^2$, $1.14 \times 10^8 \text{ A/m}^2$ and $1.40 \times 10^8 \text{ A/m}^2$, the corrosion potential of the Inconel 625 layer is improved compared to that of traditional laser deposited Inconel 625 layers.

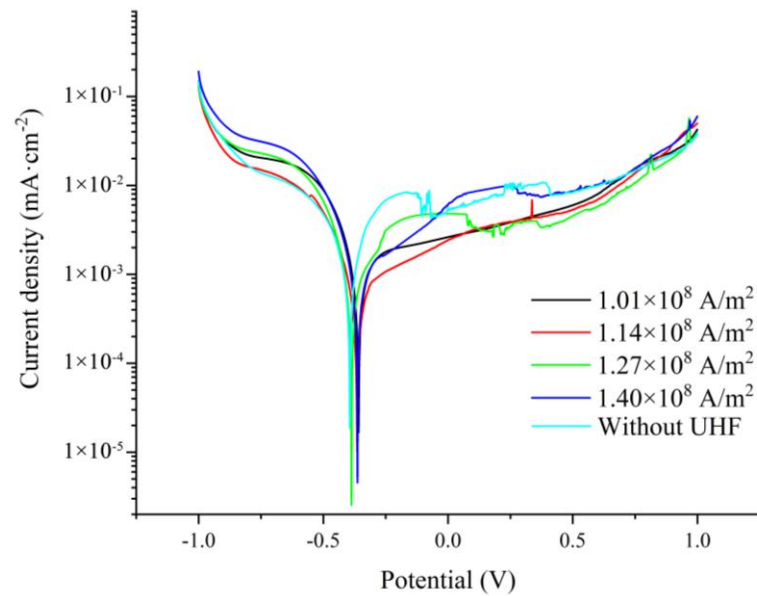


Figure 14. Polarization curves of the laser–UHF induction hybrid deposited layers under different current densities.

Table 3. Corrosion data of the tested samples under different current densities.

Current Density (A/m^2)	E_{corr} (mV)	I_{corr} ($\text{mA}\cdot\text{cm}^{-2}$)	E_b (mV)
1.01×10^8	-359	1.61×10^{-3}	548
1.14×10^8	-365	9.24×10^{-3}	585
1.27×10^8	-394	1.09×10^{-3}	353
1.40×10^8	-363	1.48×10^{-4}	382
Without UHF	-387	2.03×10^{-2}	277

Apart from corrosion potential, corrosion current density also reflects the corrosion resistance of the deposited layers. As shown in Table 3, it can be seen that the laser deposited layer has the highest corrosion current density of $2.03 \times 10^{-2} \text{ mA/cm}^2$, meaning that the corrosion speed of this layer during the corrosion test is faster than that of the laser-UHF induction hybrid deposited layer. In addition, it is noticed that, though the laser-UHF induction hybrid deposited layer prepared with a current density of $1.27 \times 10^8 \text{ A/m}^2$ has the lowest corrosion potential, its corrosion current density is relatively low at $1.09 \times 10^{-3} \text{ mA/cm}^2$. This indicates that this layer corrodes slowly. Among all the layers, the laser-UHF induction hybrid deposited layer obtained with a current density of $1.40 \times 10^8 \text{ A/m}^2$ has the smallest corrosion current density of $1.48 \times 10^{-4} \text{ mA/cm}^2$.

During the corrosion test, a dense passive film is formed at the surface of the deposited layer, which will protect it from further corrosion. This process manifests as an obvious

potential increase, with a slight increase in corrosion current density. Due to the continuous increase in potential, the passive film is destroyed by pitting corrosion. Figure 15 shows an SEM image of the pitting corrosion at the surface of the tested layer. It can be seen that there are extensive pits, which tend to expand and join together. Previous research has shown that deposited layers with low breaking-down potential are easily pitting corroded [27]. According to Table 3, the laser-UHF induction hybrid deposited layer obtained with a current density of $1.14 \times 10^8 \text{ A/m}^2$ has the highest breakdown potential of 585 mV. As for the laser deposited layer, there is a significant decrease in breakdown potential, which is 277 mV. This means that the laser deposited layer is more easily destroyed by pitting corrosion. Based on the analysis of the polarization curves, it can be derived that, with the addition of UHF induction heat, the corrosion resistance of the deposited layer is significantly improved. In addition, the deposited layer obtained with a current density of $1.01 \times 10^8 \text{ A/m}^2$ has a high corrosion potential and breakdown potential and a small corrosion current density, indicating a better corrosion resistance compared with other deposited layers.

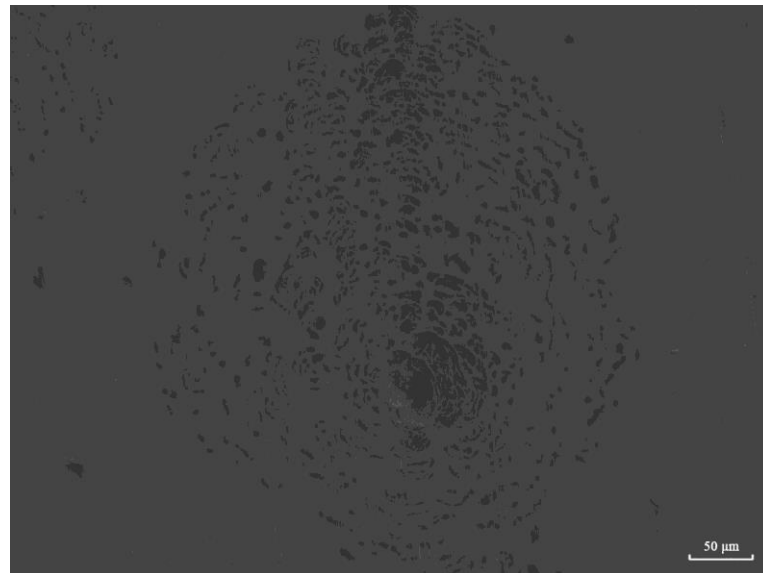


Figure 15. SEM image of pitting corrosion.

Electrochemical impedance spectroscopy (EIS) will illustrate the impedance characteristic of the equivalent electrochemical system formed by the electrolyte solution and the surface of the deposited layer. Based on the EIS results, the Nyquist plot and Bode plot are depicted in Figures 16 and 17, respectively. The Nyquist plot shown in Figure 16 exhibits a semi-circular arc shape. This demonstrates that the corrosion process is characterized by capacitive behavior, with charge transfer as the controlling step [28]. The radius of the Nyquist plot can also indicate the corrosion resistance of the deposited layer. The larger the radius of the Nyquist plot, the better the corrosion resistance of the deposited layer. It can be seen that the Nyquist plot of the deposited layer fabricated with a current density of $1.01 \times 10^8 \text{ A/m}^2$ has the largest arc radius, demonstrating a better corrosion resistance, while the Nyquist plot of the laser deposited layer has the smallest arc radius, i.e., a worse corrosion resistance. In Figure 17a, the value represented by the left end point of each curve depicts the impedance magnitude of the layer surface, and the value of the laser deposited layer is significantly lower than that of the laser-UHF induction hybrid deposited layers. Figure 17b describes the relationship between frequency and phase angle according to the EIS results. The frequency range corresponding to the maximum phase angle demonstrates the stability of the passive film formed on the surface of the deposited layer, a wide frequency range indicating a stable passive film [29]. As shown in Figure 17b, for the laser deposited layer, the frequency range corresponding to the maximum phase angle

is narrower than that of the laser-UHF induction hybrid deposited layers, and the phase angle obviously decreases in the low frequency range. This means that the passive film is easily destroyed, and this conclusion is also consistent with the analysis of the polarization curves. In order to quantitatively analyze the impedance characteristic of each layer, the EIS results are fitted by the Z-view commercial software in accordance with the equivalent circuit shown in Figure 18, and the fitted results are listed in Table 4. R_s represents the ohm resistance of the electrolyte solution, which should be less than $10 \Omega \cdot \text{cm}^2$ to ensure a good conductivity. The value of $(R_f + R_{ct})$ indicates the ohm resistance of the passive film of the deposited layer. Based on the EIS fitting results, it can be seen that the deposited layer with a current density of $1.01 \times 10^8 \text{ A/m}^2$ has the largest ohm resistance of $4.31 \times 10^4 \Omega \cdot \text{cm}^2$, while the ohm resistance of the laser deposited layer is only $1.60 \times 10^4 \Omega \cdot \text{cm}^2$. According to the value of $(R_f + R_{ct})$, the corrosion resistance of the deposited layers is in the order: deposited layer with current density of $1.01 \times 10^8 \text{ A/m}^2 > 1.40 \times 10^8 \text{ A/m}^2 > 1.14 \times 10^8 \text{ A/m}^2 > 1.27 \times 10^8 \text{ A/m}^2 >$ laser deposited layer.

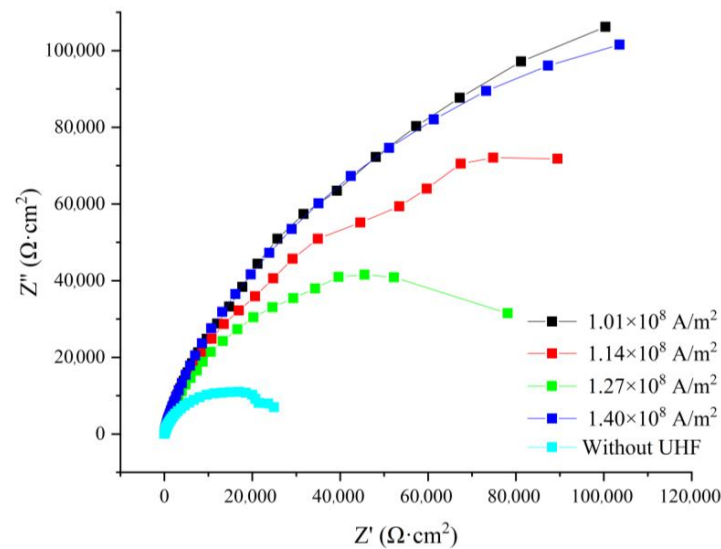
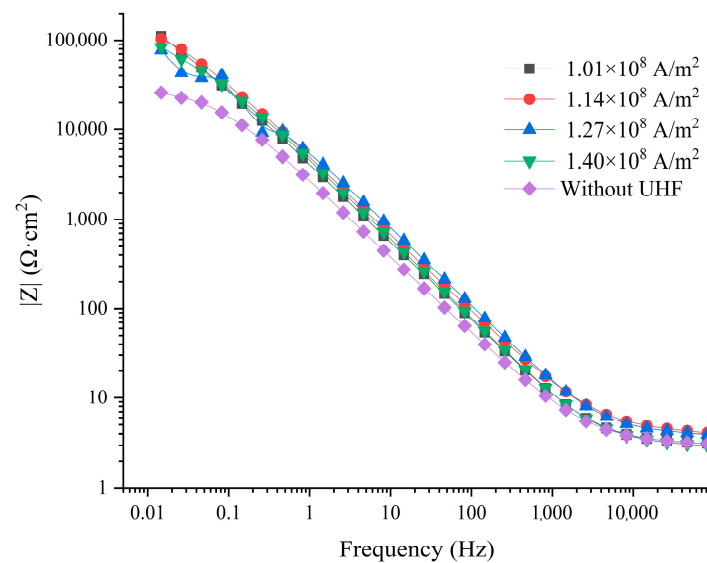


Figure 16. EIS spectra as Nyquist plot of the laser-UHF induction hybrid deposited layers under the current density.



(a)

Figure 17. Cont.

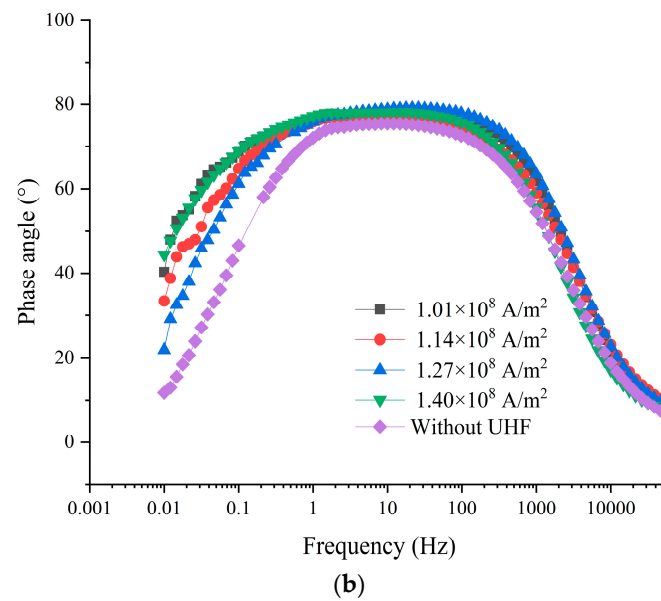


Figure 17. EIS spectra as Bode plot of the laser-UHF induction hybrid deposited layers under the current density: (a) frequency vs. amplitude (b) frequency vs. phase angle.

Based on the above analysis, it can be concluded that the addition of UHF in the laser deposition process is helpful in improving the corrosion performance of the deposited Inconel 625 layer. The analysis on wear resistance indicates that the deposited layer exhibits the lowest friction coefficient and wear rate under a current density of $1.40 \times 10^8 \text{ A/m}^2$. As far as corrosion and wear performance are concerned, the current density of $1.40 \times 10^8 \text{ A/m}^2$ is an optimal parameter for the fabrication of the Inconel 625 layer.

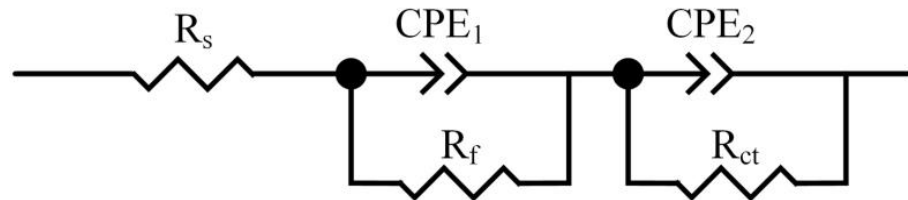


Figure 18. Equivalent circuit of EIS spectra.

Table 4. EIS fitting results of the tested samples under different current densities.

Current Density (A/m ²)	R_s ($\Omega \cdot \text{cm}^2$)	R_f ($\Omega \cdot \text{cm}^2$)	R_{ct} ($\Omega \cdot \text{cm}^2$)	CPE_1 (F/cm ²)	n_1	CPE_2 (F/cm ²)	n_2
1.01×10^8	1.839	1.54×10^4	2.77×10^4	3.39×10^{-4}	0.7261	1.57×10^{-3}	0.7367
1.14×10^8	2.730	1.58×10^4	7.23×10^3	3.50×10^{-4}	0.8017	1.74×10^{-4}	0.7903
1.27×10^8	2.777	1.85×10^4	5.03×10^2	2.47×10^{-4}	0.7411	5.45×10^{-4}	0.7572
1.40×10^8	1.848	5.99×10^3	3.57×10^4	5.51×10^{-4}	0.9358	3.06×10^{-4}	0.7141
Without UHF	1.878	1.45×10^4	1.48×10^3	1.40×10^{-4}	0.8005	1.69×10^{-2}	0.6674

4. Conclusions

In order to overcome the microstructure degradation induced by the introduction of low frequency induction heat in the laser deposition process, ultra-high frequency (UHF) induction heat was introduced to the laser deposition process to form the laser-UHF induction hybrid deposition method. The microstructure of the laser-UHF induction hybrid

deposited layer with different current densities was analyzed and compared with that of the laser deposited layer. The wear resistance and corrosion resistance of the laser-UHF induction hybrid deposited layers were also evaluated to examine the feasibility of the laser-UHF induction hybrid deposition method. The conclusions are drawn as follows.

(1) Due to the intensive electromagnetic field generated by UHF induction heat, the deposited layer fabricated with a current density of $1.14 \times 10^8 \text{ A/m}^2$ exhibits a finer microstructure than that of the laser deposited layer; and the addition of UHF induction heat is also helpful in inhibiting the segregation of Nb and Mo, reducing the amount of Laves phase in the deposited layer.

(2) From the bottom region to the top region of the laser-UHF induction hybrid deposited layer, the microstructure morphology evolves from epitaxial elongated columnar grains to columnar grains with secondary dendrite arms, and then to equiaxed grains. As the current density changes from $1.01 \times 10^8 \text{ A/m}^2$ to $1.14 \times 10^8 \text{ A/m}^2$, the grain size of the deposited layer is significantly refined; however, when the current density further increases, the microstructure of the deposited layer is only slightly refined, which may be attributed to the increasing thermal effect, along with the increasing current density.

(3) The wear test results indicate that, under a current density of $1.40 \times 10^8 \text{ A/m}^2$, the laser-UHF induction hybrid deposited layer has the lowest average friction coefficient and wear rate, exhibiting the best wear resistance; while the deposited layer fabricated with a current density of $1.01 \times 10^8 \text{ A/m}^2$ has the worst wear resistance. The morphology of the wear surface indicates that the laser-UHF induction hybrid deposited layer under current densities of $1.14 \times 10^8 \text{ A/m}^2$ and $1.40 \times 10^8 \text{ A/m}^2$ exhibits abrasive wear and adhesive wear, and other layers exhibit abrasive wear.

(4) The corrosion resistance can be improved by the addition of UHF induction heat, and the laser-UHF induction hybrid deposited layer obtained with a current density of $1.01 \times 10^8 \text{ A/m}^2$ has the highest ohm resistance for the passive film, indicating the best corrosion resistance. In terms of corrosion and wear performance, the current density of $1.40 \times 10^8 \text{ A/m}^2$ is an optimal parameter for the laser-UHF induction hybrid deposited Inconel 625 layer.

Author Contributions: Conceptualization, R.S.; investigation, R.S. and Y.Q.; supervision, Y.S. and X.L.; visualization, R.S. and Y.Q.; writing—original draft, R.S.; writing—review and editing, R.S. and X.W. All authors have read and agreed to the published version of the manuscript.

Funding: This work was financially supported by the National Natural Science Foundation of China (No. 52105456).

Institutional Review Board Statement: Not applicable.

Informed Consent Statement: Not applicable.

Data Availability Statement: Not applicable.

Conflicts of Interest: The authors declare no conflict of interest.

References

1. Rahman Rashid, R.A.; Barr, C.J.; Palanisamy, S.; Nazari, K.A.; Orchowski, N.; Matthews, N.; Dargusch, M.S. Effect of clad orientation on the mechanical properties of laser-clad repaired ultra-high strength 300 M steel. *Surf. Coat. Tech.* **2019**, *380*, 125090. [[CrossRef](#)]
2. Cailloux, T.; Pacquentin, W.; Narasimalu, S.; Belnou, F.; Schuster, F.; Maskrot, H.; Wang, C.C.; Zhou, K.; Balbaud-Celerier, F. Influence of trapezoidal groove geometry on the microstructure and mechanical properties of stainless steel 316L parts repaired by laser metal deposition. *Mat. Sci. Eng. A-Struct.* **2022**, *859*, 144218. [[CrossRef](#)]
3. Zhu, S.C.; Chen, W.L.; Zhan, X.H.; Ding, L.P.; Zhou, J.J. Parameter optimisation of laser cladding repair for an Invar alloy mould. *P. I. Mech. Eng. B-J. Eng.* **2019**, *233*, 1859–1871. [[CrossRef](#)]
4. Segerstark, A.; Andersson, J.; Svensson, L.E.; Ojo, O. Effect of process parameters on the crack formation in laser metal powder deposition of alloy 718. *Metall. Mater. Trans. A* **2018**, *49*, 5042–5050. [[CrossRef](#)]
5. Gao, Z.N.; Wang, L.L.; Wang, Y.N.; Lyu, F.Y.; Zhan, X.H. Crack defects and formation mechanism of FeCoCrNi high entropy alloy coating on TC4 titanium alloy prepared by laser cladding. *J. Alloys Compd.* **2022**, *903*, 163905. [[CrossRef](#)]

6. Sadhu, A.; Choudhary, A.; Sarkar, S.; Nair, A.M.; Nayak, P.; Pawar, S.D.; Muvvala, G.; Pal, S.K. A study on the influence of substrate pre-heating on mitigation of cracks in direct metal laser deposition of NiCrSiBC-60%WC ceramic coating on Inconel 718. *Surf. Coat. Tech.* **2020**, *389*, 125646. [[CrossRef](#)]
7. Zhou, S.F.; Dai, X.Q. Laser induction hybrid rapid cladding of WC particles reinforced NiCrBSi composite coatings. *Appl. Surf. Sci.* **2010**, *256*, 4708–4714. [[CrossRef](#)]
8. Huang, Y.J.; Zeng, X.Y. Investigation on cracking behavior of Ni-based coating by laser-induction hybrid cladding. *Appl. Surf. Sci.* **2010**, *256*, 5985–5992. [[CrossRef](#)]
9. Farahmand, P.; Kovacevic, R. Laser cladding assisted with an induction heater (LCAIH) of Ni-60%WC coating. *J. Mater. Process Tech.* **2015**, *222*, 244–258. [[CrossRef](#)]
10. Dalaei, M.T.; Gloor, L.; Leinenbach, C.; Wegener, K. Experimental and numerical study of the influence of induction heating process on build rates induction heating-assisted laser direct metal deposition (IH-DMD). *Surf. Coat. Tech.* **2020**, *384*, 125275. [[CrossRef](#)]
11. Meng, L.; Zhao, W.F.; Hou, K.L.; Kou, D.H.; Yuan, Z.H.; Zhang, X.; Xu, J.L.; Hu, Q.W.; Wang, D.Z.; Zeng, X.Y. A comparison of microstructure and mechanical properties of laser cladding and laser-induction hybrid cladding coatings on full-scale. *Mat. Sci. Eng. A-Struct.* **2019**, *748*, 1–15. [[CrossRef](#)]
12. Wang, X.Y.; Zhou, S.F.; Dai, X.Q.; Lei, J.B.; Guo, J.B.; Gu, Z.J.; Wang, T. Evaluation and mechanisms on heat damage of WC particles in Ni60/WC composite coatings by laser induction hybrid cladding. *Int. J. Refract. Met. H* **2017**, *64*, 234–241. [[CrossRef](#)]
13. Zhou, S.F.; Lei, J.B.; Dai, X.Q.; Guo, J.B.; Gu, Z.J.; Pan, H.B. A comparative study of the structure and wear resistance of NiCrBSi/50wt.% WC composite coatings by laser cladding and laser induction hybrid cladding. *Int. J. Refract. Met. H* **2016**, *60*, 17–27. [[CrossRef](#)]
14. Lu, L.L.; Zhang, S.M.; Xu, J.; He, H.J.; Zhao, X.M. Numerical study of titanium melting by high frequency inductive heating. *Int. J. Heat Mass. Tran.* **2017**, *108*, 2021–2028. [[CrossRef](#)]
15. Li, Q.L.; Su, H.H.; Xu, J.H.; Lei, W.N. Interfacial Microstructure and Residual Stress of Continuously Brazed Diamond with Ag-Cu-Ti Alloy Using Ultra-high Frequency Induction. *Rare Metal Mat. Eng.* **2017**, *45*, 3250–3254.
16. Huang, C.Y.; Lin, Y.C.; Chen, H.M.; Chen, Y.C. Rapid welding of stainless steel wires using ultra-high frequency induction heating. *J. Chin. Inst. Eng.* **2013**, *36*, 806–809. [[CrossRef](#)]
17. Altintas, A.; Cavdar, U.; Kusoglu, I.M. The Effect of Graphene Nanoplatelets on the Wear Properties of High-Frequency Induction Sintered Alumina Nanocomposites. *J. Inorg. Organomet. P.* **2019**, *29*, 667–675. [[CrossRef](#)]
18. Bai, X.W.; Hai, H.O.; Zhou, X.M.; Wang, G.L. Electromagneto-fluid Coupling Simulation of Arc Rapid Prototyping Process with External High-frequency Magnetic Field. *J. Mech. Eng.* **2016**, *52*, 60–66. [[CrossRef](#)]
19. Meng, X.M.; Bachmann, M.; Artinov, A.; Rethmeier, M. Experimental and numerical assessment of weld pool behavior and final microstructure in wire feed laser beam welding with electromagnetic stirring. *J. Manuf. Process.* **2019**, *45*, 408–418. [[CrossRef](#)]
20. Liu, F.C.; Cheng, H.M.; Yu, X.B.; Yang, G.; Huang, C.P.; Lin, X.; Chen, J. Control of microstructure and mechanical properties of laser solid formed Inconel 718 superalloy by electromagnetic stirring. *Opt. Laser Technol.* **2018**, *99*, 342–350. [[CrossRef](#)]
21. Wang, Z.D.; Zhou, H.M.; Chen, Z.X.; Zhu, Y.X.; He, F.J.; Xiang, N.X.; Wang, Y.H. Study on the effect of electromagnetic field on the segregation and structural property of Ni60 cladding layer. *Optik* **2023**, *272*, 170279. [[CrossRef](#)]
22. Hao, J.B.; Hu, F.T.; Le, X.W.; Liu, H.; Yang, H.F.; Han, J. Microstructure and high-temperature wear behaviour of Inconel 625 multi-layer cladding prepared on H13 mould steel by a hybrid additive manufacturing method. *J. Mater. Process Tech.* **2021**, *291*, 117036. [[CrossRef](#)]
23. Ramkumar, K.D.; Mulimani, S.S.; Ankit, K.; Kothari, A.; Ganguly, S. Effect of grain boundary precipitation on the mechanical integrity of EBW joints of Inconel 625. *Mat. Sci. Eng. A-Struct.* **2021**, *808*, 140926. [[CrossRef](#)]
24. Sarswat, P.; Smith, T.; Sarkar, S.; Murali, A.; Free, M. Design and Fabrication of New High Entropy Alloys for Evaluating Titanium Replacements in Additive Manufacturing. *Materials* **2020**, *13*, 3001. [[CrossRef](#)]
25. Poloczek, T.; Lont, A.; Gorka, J. The Structure and Properties of Laser-Cladded Inconel 625/TiC Composite Coatings. *Materials* **2023**, *16*, 1265. [[CrossRef](#)] [[PubMed](#)]
26. Rezayat, M.; Sani, A.A.; Noghani, M.T.; Yazdi, M.S.; Taheri, M.; Moghanian, A.; Mohammadi, M.A.; Moradi, M.; Garcia, A.M.M.; Besharatloo, H. Effect of Lateral Laser-Cladding Process on the Corrosion Performance of Inconel 625. *Metals* **2023**, *13*, 367. [[CrossRef](#)]
27. Sarswat, K.P.; Sarkar, S.; Murali, A.; Huang, W.K.; Tan, W.D.; Free, M.L. Design, fabrication and evaluation of Fe-Mn-Mo-Zr-Ti-V-B type additive manufactured mixed metal boride ceramics. *Appl. Surf. Sci. Adv.* **2022**, *9*, 100247. [[CrossRef](#)]
28. Jiang, D.; Cui, H.Z.; Chen, H.; Song, X.J.; Zhao, X.F.; Xie, J.C.; Ma, G.L. Wear and corrosion resistance improvement of $(\text{CoCrNi})_{72-x}\text{B}_{18}\text{Si}_{10}\text{Nb}_x$ coatings obtained by laser cladding: Role of Nb concentration. *Mater. Today. Commun.* **2022**, *34*, 105057. [[CrossRef](#)]
29. Osorio, W.R.; Peixoto, L.C.; Moutinho, D.J.; Gomes, L.G.; Ferreira, I.L.; Garcia, A. Corrosion resistance of directionally solidified Al-6Cu-1Si and Al-8Cu-3Si alloys castings. *Mater. Design.* **2011**, *32*, 3832–3837. [[CrossRef](#)]

Disclaimer/Publisher's Note: The statements, opinions and data contained in all publications are solely those of the individual author(s) and contributor(s) and not of MDPI and/or the editor(s). MDPI and/or the editor(s) disclaim responsibility for any injury to people or property resulting from any ideas, methods, instructions or products referred to in the content.